Supplementary Information for "Droplets sliding on soft solids shed elastocapillary rails"

Nan Xue,[1,2,3] Lawrence A. Wilen,[4] Robert W. Style,[1,*] and Eric R. Dufresne[1,2,3,†]

[1]*Department of Materials, ETH Zürich, 8093 Zürich, Switzerland.*

[2]*Department of Materials Science and Engineering,*

Cornell University, Ithaca, NY, 14853, USA.

[3]*Laboratory of Atomic and Solid-State Physics,*

Cornell University, Ithaca, NY, 14853, USA.

[4]*Center for Engineering Innovation and Design,*

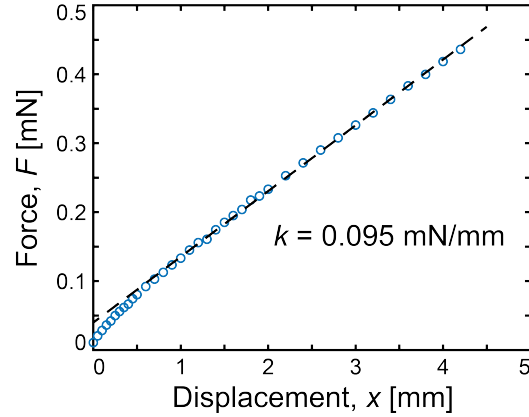*School of Engineering and Applied Sciences, Yale University, NH, 06520, USA.*

(Dated: November 25, 2024)

**Schematic of the Experimental Setup**
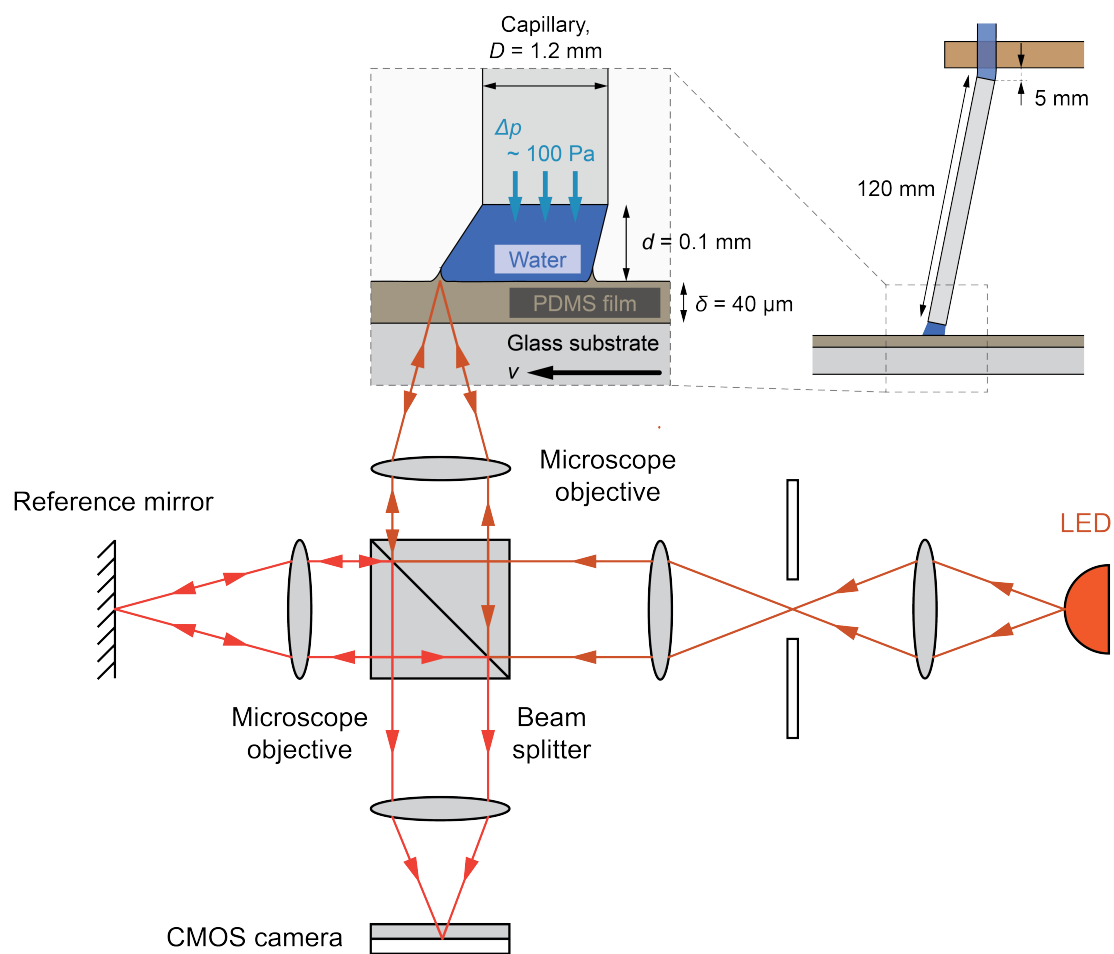
Supplementary Information Fig. 1.   Schematic diagram of the experimental setup, featuring a Linnik interference microscope for high-resolution imaging of the PDMS interface.

Calibration of the Force Measurement

Supplementary Information Fig. 2. The calibration curve that shows the linear relationship between applied force and capillary displacement. The experimental setup consists of a capillary connected to a PVC tube, which is, in turn, attached to a linear actuator. This setup effectively translates tube deformation (the deformation is mainly due to the bending of the PVC tube; the capillary remains uncurved) into a measurable force, allowing for precise control of the applied force on the droplet. By adjusting the length of the PVC tube, we can readily tune the effective spring constant of the system. The system is calibrated by reorienting the capillary horizontally, attaching its free end to a balance, and measuring the force response as the actuator-controlled end of the tube is vertically displaced. The dashed line represents a linear fit to the calibration data, yielding a spring constant of $k = 0.095 \pm 0.002$ mN/mm. A small offset is observed in the low-force regime, likely attributable to minor gravitational effects arising from slight deviations from perfect vertical alignment of the capillary. Nonetheless, the linear fit demonstrates the reliable and tunable force response of the system, which is crucial for accurate measurements of the forces acting on the sliding droplet.

Dissipation Rate
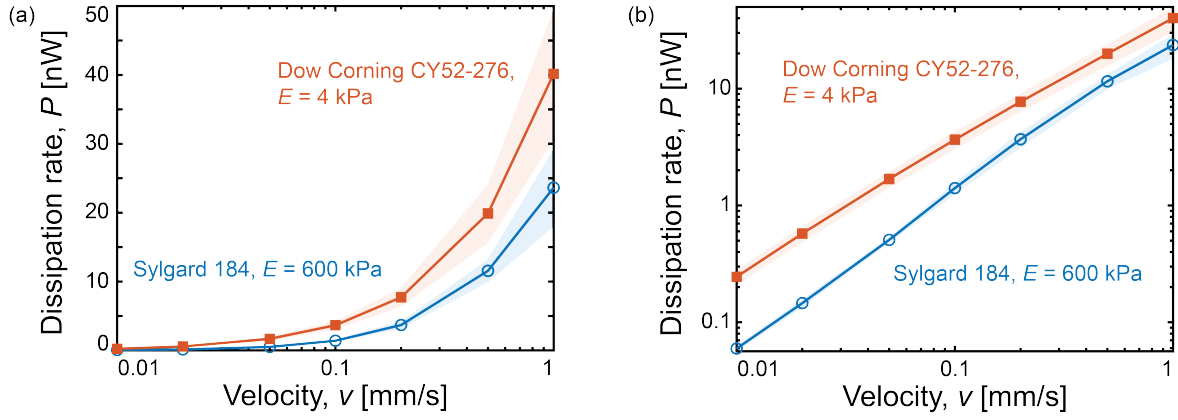
Supplementary Information Fig. 3. (a) The energy dissipation rate $P(= Fv)$ of the sliding droplets as a function of velocity. (b) Log-log plot of the energy dissipation rate data presented in panel (a). The colored shadow represents the standard deviation across three experiments.

Droplet Shapes
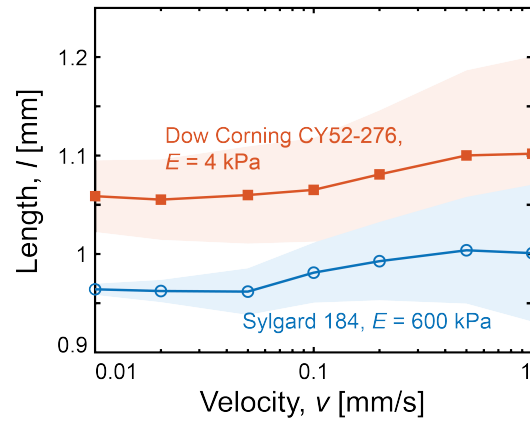
Supplementary Information Fig. 4. The length l of the droplets as a function of velocity. The colored shadow represents the standard deviation across three experiments.

Estimation of Dissipation Using the 2D Viscoelastic Model

We summarize the linear viscoelastic model from Ref. 1, used to estimate the dissipation represented by the dashed lines in Figs. 1(c) and 3 of the main manuscript. This model focuses on the static shape of the wetting ridge and employs spatial Fourier transformations. For brevity, we present the key equations necessary for reproducing the estimation; interested readers can refer to Ref. 1 for a complete discussion.

The contact angle of water on our PDMS film is $\theta \approx 90°$. We are primarily interested in the change in contact angle φ due to the wetting ridge during droplet movement, as $\gamma \sin \varphi$ provides a direct estimate of the dissipative force per unit width of the contact line (where $\gamma = 70$ mN/mm is the surface tension of water).

Equation (22) in Ref. 1 expresses φ as

$$\tan \varphi = \frac{1}{\pi} \int_{-\infty}^{\infty} \mathcal{R} \left[-iq\tilde{h}\left(q\right) \right] \mathrm{d}q, \tag{1}$$

where $\mathcal{R}[...]$ denotes the real part, q is the wave number, and $\tilde{h}$ is the film thickness in the spatial Fourier domain.

Equation (7) in Ref. 1 provides the expression for $\tilde{h}$:

$$\tilde{h} = \frac{\gamma \sin \theta}{\gamma_\mathrm{s}} \left[q^2 + \frac{G^*\left(qv\right)/\gamma_\mathrm{s}}{K(q)} \right]^{-1}, \tag{2}$$

where $\gamma_\mathrm{s} = 30$ mN/mm is the surface tension of the soft substrate [2], v is the droplet velocity, $K(...)$ is the space kernel, and $G^*(...)$ is the viscoelastic property of the substrate. Following Refs. 1, 2, we model the complex modulus of the softer gel using the power-law form $G^*(\omega) = G_0[1 + (i\omega\tau)^n]$ with shear modulus $G_0 = 1.3$ kPa, intrinsic timescale $\tau = 0.11$ s, and power $n = 0.54$. For thick substrates, the space kernel is given by Eq. (5) in Ref. 1:

$$K(q) = \left(2\left|q\right|\right)^{-1}. \tag{3}$$

By substituting the physical parameters into Eqs. 1, 2, and 3, we obtain the value of φ. The dissipative force per unit width of the contact line is then $\gamma \sin \varphi$. In the main manuscript, we double this value to account for both advancing and receding fronts.

In our experiments, the sample thickness ($\delta = 40$ μm) is several times larger than the elastocapillary length (γ/E), but still within the same order of magnitude. To account for this finite thickness effect, we incorporate the modified space kernel from Ref. 1:

$$K(q) = \left[\frac{\sinh(2q\delta) - 2q\delta}{\cosh(2q\delta) + 2(q\delta)^2 + 1} \right] \frac{1}{2q}. \tag{4}$$
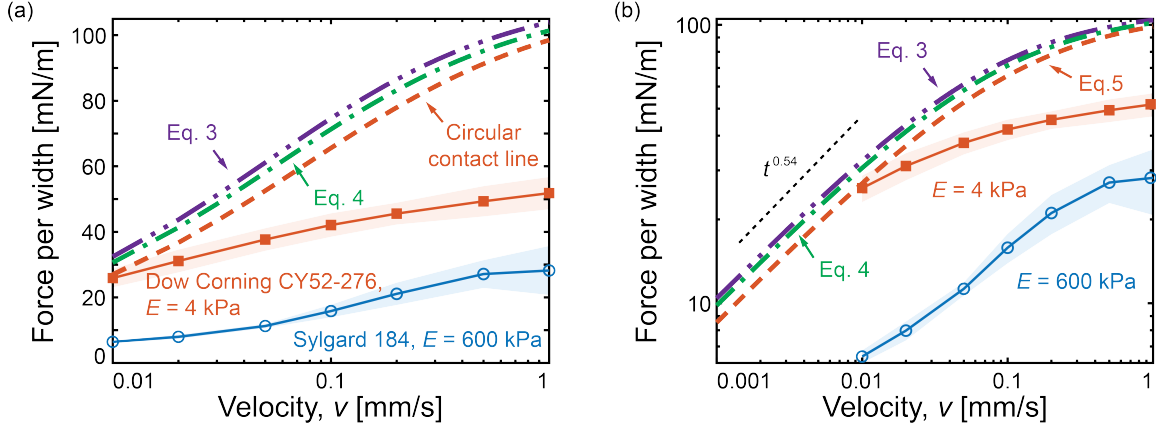
Supplementary Information Fig. 5. (a) Estimated force per unit width of the moving droplet as a function of velocity (v). The dashed lines represent model estimations using Eq. 3 (top), Eq. 4 (middle), and Eq. 5 (bottom). (b) Log-log plot of the force per unit width data presented in panel (a).

Using Eq. 4 in conjunction with Eqs. 1 and 2 slightly reduces the estimated dissipation (see Fig. S5).

In Fig. S5, the purple and green dashed lines represent the model predictions from Eq. 3 and Eq. 4, respectively. These predictions assume a simplified scenario where the contact line is treated as a straight line moving at a uniform velocity, v, for the force per unit length calculation. Next, we refine our analysis by incorporating the more realistic circular shape of the contact line. Since only the velocity component perpendicular to the contact line contributes to dissipation, the force per unit droplet width is given by:

$$F/w = \gamma \int_{-\pi/2}^{\pi/2} \cos\alpha \sin\varphi(v\cos\alpha)\mathrm{d}\alpha, \tag{5}$$

where $\varphi(...)$ is determined by Eq. 1. This correction for the contact line shape is illustrated in Fig. S5 and shows a tiny modification on the results.

We also plot the log-log relationship between the force per unit width and the velocity in Fig. S5(b). The linear viscoelastic model predicts that the force per unit width scales as v^n [1], where $n = 0.54$. Indeed, such asymptotic trend is observed in our model estimation, up to $v = 0.01$ mm/s. Our experimental results are limited to velocities greater than $v = 0.01$ mm/s, so these experiments provide ready access to the theoretical low-velocity asymptotic limit.

7

Quantifying Surface Topography with Phase Retrieval

The interferometric fringes reveal the underlying surface topography, which we quantify using phase retrieval methods [3–5]. This approach, also employed in our previous work to analyze dimple relaxation [2], involves applying a 2D Fourier transform to the fringe pattern within a carefully selected region of interest. A rectangular window is cropped from the Fourier transform image, with its size optimized to ensure the robustness of the results. This optimization involves systematically varying the window size and selecting the range where the final results are insensitive to further changes. The inverse Fourier transform is then applied to generate the phase map, which is unwrapped to obtain the surface height profile.

A demonstration code (generating step-by-step results including figures) and example images are provided in the Supplementary Information.
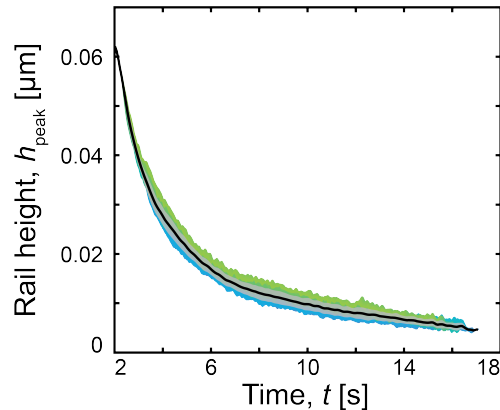
Supplementary Information Fig. 6. Relaxation of elastocapillary rail peak height over time for a droplet moving at 0.5 mm/s. Data points (colored by position along the rail within a 2 mm spread) represent individual measurements (737 in total), while the solid black line and shaded region indicate the mean and standard deviation, respectively.

Using phase retrieval methods, we obtain the peak height of the elastocapillary rails as a function of both time and position along the rail. Different positions correspond to different relaxation times since the rails detach from the droplet contact line at various points. Notably, the rail height measurements collapse when plotted against the time elapsed since detachment from the contact line, as shown in Fig. S6. This collapse demonstrates the robustness of our phase retrieval processing and can also be used to estimate processing

errors.
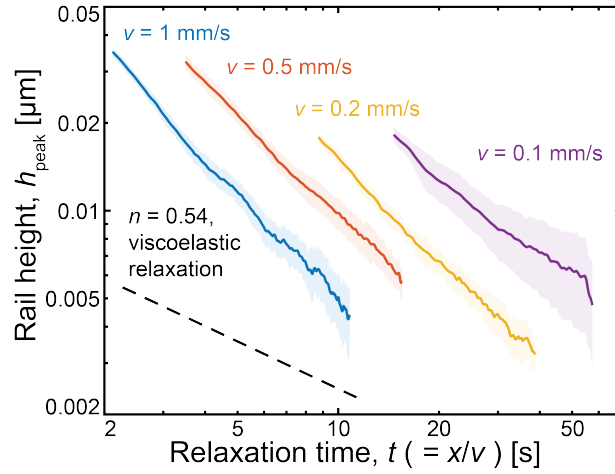
Supplementary Information Fig. 7.   Relaxation of the rail height h_{peak} over time, t. The colored shadow shows the standard deviation described in Fig. S6.

Figure 4 in the main manuscript presents the relaxation of rail height at various sliding speeds for a single sample. Here, Fig. S7 demonstrates a similar relaxation behavior for a different sample prepared using the same protocol. This consistency across samples further supports the robustness of the observed phenomenon.

List of Movies

Movie 1: Side view of a droplet moving at 1 mm/s on a soft ($E = 4$ kPa) PDMS film (real-time playback).

Movie 2: Interferometric view of a droplet moving slowly at 0.01 mm/s on a stiff ($E = 600$ kPa) PDMS film (20x real-time playback).

Movie 3: Interferometric view of a droplet moving rapidly at 1 mm/s on a stiff ($E = 600$ kPa) PDMS film (real-time playback).

Movie 4: Interferometric view of a droplet moving slowly at 0.01 mm/s on a soft ($E = 4$ kPa) PDMS film (20x real-time playback).

Movie 5: Interferometric view of a droplet moving rapidly at 1 mm/s on a soft ($E = 4$ kPa) PDMS film (real-time playback).

Movie 6: Interferometric view of another droplet moving rapidly at 1 mm/s on a soft ($E = 4$ kPa) PDMS film (real-time playback).

* robert.style@mat.ethz.ch

† eric.r.dufresne@cornell.edu

[1] S. Karpitschka, S. Das, M. van Gorcum, H. Perrin, B. Andreotti, and J. H. Snoeijer, Droplets move over viscoelastic substrates by surfing a ridge, Nat. Commun. **6**, 7891 (2015).

[2] Q. Xu, L. A. Wilen, K. E. Jensen, R. W. Style, and E. R. Dufresne, Viscoelastic and poroelastic relaxations of soft solid surfaces, Phys. Rev. Lett. **125**, 238002 (2020).

[3] M. Takeda, H. Ina, and S. Kobayashi, Fourier-transform method of fringe-pattern analysis for computer-based topography and interferometry, J. Opt. Soc. Am. **72**, 156 (1982).

[4] M. A. Herráez, D. R. Burton, M. J. Lalor, and M. A. Gdeisat, Fast two-dimensional phase-unwrapping algorithm based on sorting by reliability following a noncontinuous path, Appl. Opt. **41**, 7437 (2002).

[5] M. F. Kasim, Fast 2D phase unwrapping implementation in MATLAB (2017).